

Machine learning for graph-based representations of three-dimensional discrete fracture networks

Manuel Valera · Zhengyang Guo ·
Priscilla Kelly · Sean Matz ·
Adrian Cantu · Allon G. Percus ·
Jeffrey D. Hyman · Gowri Srinivasan ·
Hari S. Viswanathan

the date of receipt and acceptance should be inserted later

M. Valera

Computational Science Research Center, San Diego State University, San Diego, CA 92182,
United States of America, and Institute of Mathematical Sciences, Claremont Graduate
University, Claremont, CA 91711, United States of America,

Z. Guo

Institute of Mathematical Sciences, Claremont Graduate University, Claremont, CA 91711,
United States of America

P. Kelly

Computational Science Research Center, San Diego State University, San Diego, CA 92182,
United States of America, and Institute of Mathematical Sciences, Claremont Graduate
University, Claremont, CA 91711, United States of America,

S. Matz

Institute of Mathematical Sciences, Claremont Graduate University, Claremont, CA 91711,
United States of America

A. Cantu

Computational Science Research Center, San Diego State University, San Diego, CA 92182,
United States of America, and Institute of Mathematical Sciences, Claremont Graduate
University, Claremont, CA 91711, United States of America,

A. G. Percus

Institute of Mathematical Sciences, Claremont Graduate University, Claremont, CA 91711,
United States of America

J. D. Hyman

Computational Earth Science Group (EES-16), Earth and Environmental Sciences Division,
Los Alamos National Laboratory, Los Alamos, NM 87545, United States of America *Corre-*
sponding Author E-mail: jhyman@lanl.gov

G. Srinivasan

Applied Mathematics and Plasma Physics (T-5), Theoretical Division, Los Alamos National
Laboratory, Los Alamos, NM 87545, United States of America

H. S. Viswanathan

Computational Earth Science Group (EES-16), Earth and Environmental Sciences Division,
Los Alamos National Laboratory, Los Alamos, NM 87545, United States of America

Abstract Structural and topological information play a key role in modeling of flow through fractured rock. Discrete fracture network (DFN) computational suites such as DFNWORKS [23] are designed to simulate flow and transport in such media. Transport calculations that use a particle tracking method reveal that a small backbone of fractures exists where most transport occurs providing a significant reduction in the effective size of the flowing fracture network. However, the simulations needed for particle tracking are computationally intensive, and may not be scalable to large systems or for robust uncertainty quantification of fracture networks where thousands of forward simulations are needed to bound system behavior.

In this paper, we combine machine learning and graph theoretical methods to develop an emulator of DFNWORKS for quick estimates of transport that can mimic the high fidelity discrete fracture networks. We introduce a machine learning approach to characterizing transport in DFNs. We consider a graph representation where nodes signify fractures and edges denote their intersections. Using supervised learning techniques, random forest and support vector machines, that train on particle-tracking backbone paths found by DFNWORKS, we predict whether or not fractures conduct significant flow, based primarily on node centrality features in the graph. Our methods run in negligible time compared to particle-tracking simulations. We find that our predicted backbone can reduce the network to approximately 20% of its original size, while still generating breakthrough curves resembling those of the full network.

Keywords Machine learning · Discrete Fracture Networks · Support Vector Machines · Random Forest · Centrality

1 Introduction

In low permeability media, such as shales and granite, interconnected networks of fractures are the primary pathways for fluid flow and associated transport of dissolved chemicals. Characterizing flow and transport through fractured media in the subsurface is critical in many civil, industrial, and security applications including drinking water aquifer management [33], hydrocarbon extraction [19,27], carbon sequestration [26]. For example, increasing extraction efficiency from hydraulic fracturing, preventing leakage from CO₂ sequestration, or detecting the arrival time of subsurface gases from a nuclear test requires a model that can accurately simulate flow through a subsurface fracture network.

In these sparse systems fracture network topology controls system behavior but is uncertain because the exact location of subsurface fractures cannot be determined with sites often 1000s of feet below the ground. This necessitates a method to quickly calculate the transport time of solutes through realistic statistical representations of fracture networks. The topology of the network can induce flow channeling, where isolated regions of high velocity form within the network [1,2,10,11,24,39]. The formation of these flow channels indicates that

much of the flow and transport occurs in a subnetwork of the whole domain. There are techniques available to identify the fractures that make up these subnetworks, commonly referred to as the backbone [3,30]. However, these techniques require resolving flow and/or transport through the entire network prior to being able to identify the backbone. For large networks, particle-based simulations [40,44] can be costly in terms of required computational time. These costs are exacerbated because numerous network realizations are required to obtain trustworthy statistics of upscaled quantities of interest, e.g., the distribution of fracture characteristics that make up the backbone. Because the connectivity of the networks is more dominant in determining where flow occurs in sparse systems than geometric or hydraulic properties [20], it should be possible to extract the backbone using the network's topological properties.

Graph representations of fracture networks have been proposed by Ghafari, et al. [13] and independently by Andresen, et al. [4]. These graph mappings allow for a characterization of the network topology of both two- and three-dimensional fracture systems, and moreover enable quantitative comparisons between real fracture networks and models generating synthetic networks. Veatne, et al. [47] and Hope, et al. [18] have used this graph construction for analyzing fracture growth and propagation, showing how topological properties of the network such as assortativity relate to the growth mechanism. Hyman, et al. [22] used graph representations of three-dimensional fracture networks to isolate subnetworks where the fastest transport occurred by finding the shortest path between inflow and outflow boundaries. Santiago, et al. [41,42,43] proposed a method of topological analysis using a related graph representation of fracture networks. By measuring centrality properties of nodes in the graph, which describe characteristics such as the number of shortest paths through a given node, they developed a method intended to predict regions of high flow conductivity in the network.

In recent years, there has been increased interest in the use of machine learning in the geosciences. A range of different regression and classification methods have been applied to a model of landslide susceptibility, demonstrating their predictive value [14]. Community detection methods have been used in fractured rock samples to identify regions expected to have high flow conductivity [42]. Clustering analysis has been used in subsurface systems to construct more accurate flow inversion algorithms [32].

We combine these two approaches, discrete fracture network (DFN) graph representations and machine learning, to develop a classifier that learns to characterize fracture network backbones. We represent a fracture by a node in the graph, and an intersection between two fractures by an edge. Using this construction, the graph retains topological information about the network as node-based properties or features. On the basis of six features, four topological and two physical, we apply machine learning to identify the network's backbone. We use two supervised learning methods, random forest and support vector machines. Both algorithms have the advantage of being general-purpose methods, suitable for geometric as well as non-geometric features, and requiring relatively little parameter tuning. *Our overall goal is to combine machine*

learning and graph theoretical methods to mimic high-fidelity discrete fracture networks simulations for quick estimates of transport.

Under different parameter choices for random forest and SVM, we are able to reduce fracture networks on average to between 39% and 2.5% of their original number of fractures. Reductions to as little as 21% still result in a breakthrough curve in good agreement with that of the full network. Thus, our methods yield backbone subnetworks that are significantly smaller than the full network, while matching some of its flow properties. Notably, we are able to generate these backbones in seconds, as opposed to the hours of computation time needed to extract the backbone from particle-flow simulations.

We also assess the importance of the different features used to characterize the data, finding that they cluster into three natural groups. The global topological quantities are the most significant ones, followed by the one local topological quantity we use. The physical quantities are the least significant ones, though still necessary for the performance of the classifier.

In section 2, we describe the flow and transport equations used to determine particle-trace based backbones in the DFN. Section 3 describes the graph representation, as well as the features used to characterize nodes in the graph. Section 4 discusses the details of the machine learning methods used, and section 5 presents the results of these methods. Finally, in section 6, we discuss the implications of our results and provide conclusions.

2 Discrete Fracture Network

Discrete fracture networks (DFN) models are one common simulation tools used to investigate flow and transport in fractured systems. In the DFN methodology, the fracture network and hydrological properties are explicitly represented as discrete entities within an interconnected network of fractures. The inclusion of such detailed structural and hydrological properties allows DFN models to represent a wider range of transport phenomena than traditional continuum models [36,37]. In particular, topological, geometric, and hydrological characteristics can be directly linked to physical flow observables.

We use the computational suite DFNWORKS [23] to generate each DFN, solve the steady-state flow equations and determine transport properties. DFNWORKS combines the feature rejection algorithm for meshing (FRAM) [21], the LaGriT meshing toolbox [28], the parallelized subsurface flow and reactive transport code PFLOTRAN [29], and an extension of the WALKABOUT particle tracking method [31,38]. FRAM is used to generate three-dimensional fracture networks. LaGriT is used to create a computational mesh representation of the DFN in parallel. PFLOTRAN is used to numerically integrate the governing flow equations. WALKABOUT is used to determine pathlines through the DFN and simulate solute transport. Details of the suite, its abilities, applications, and references for detailed implementation are provided in [23].

One hundred generic networks, composed of circular fractures with uniformly random orientations, are generated. Each DFN lies within a cubic do-

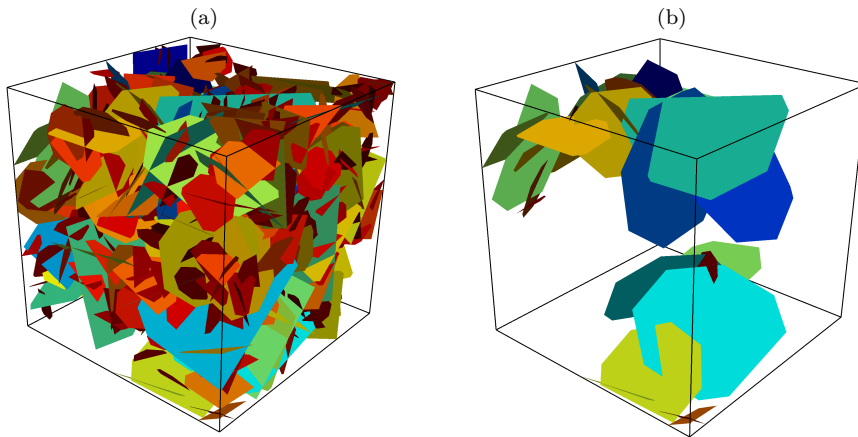


Fig. 1 (a) Full DFN composed of 499 fractures. (b) Backbone extracted from (a) using particles trajectories. Inlet plane is shown on front left; outlet plane is on rear right.

main with sides of length 15 meters. The fracture radii r [m] are sampled from a truncated power law distribution with exponent α and upper and lower cut-offs (r_u ; r_0). We select a value of $\alpha = 2.6$ so that the distribution has finite mean and variance. The lower cut off r_0 is set to one meter and the upper cut off equal r_u is set to five meters. Fracture centers are sampled uniformly throughout the domain. The networks are fairly sparse, with an average P_{32} value (fracture surface area over total volume) of $1.97 \text{ [m}^{-1}\text{]}$ and variance 0.03. In all networks, at least one set of fractures connects the inflow and outflow boundaries. This constraint removes isolated clusters that do not contribute to flow. An example of one fracture network is shown in Figure 1(a).

Within each network, the governing equations for pressure and fluid flow are numerically integrated until steady-state conditions are obtained. Purely advective particles are tracked through steady-state flow fields to simulation transport. Details of the flow and transport simulations are provided in the appendix. Particle pathlines are used to identify backbones in the DFN, connected subsets of fractures where a substantial portion of flow and transport occurs, using the methods of Aldrich, et al. [3]. Figure 1(b) shows the backbone extracted from the network shown in Figure 1(a).

3 Graph Representation

3.1 Graph Formation

We construct a graph representation of each DFN based on the network topology using the method described in Hyman, et al. [22]. For every fracture in the DFN, there is a unique node in a graph. If two fractures intersect, then there is an edge in the graph connecting the corresponding nodes. This mapping

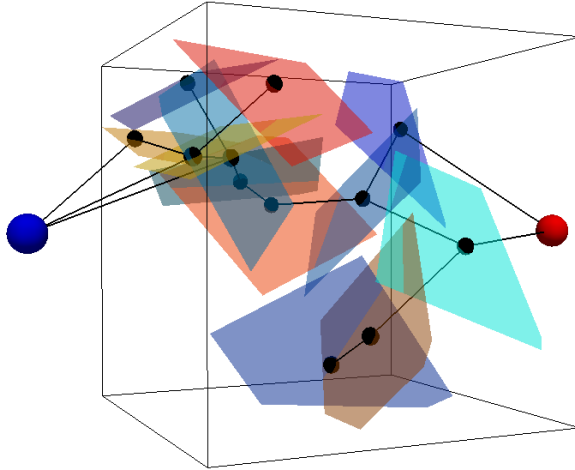


Fig. 2 Graph representation of a twelve-fracture discrete fracture network in three dimensions. Fractures (semi-transparent colored planes) are represented as nodes (black), intersections between fractures are represented by edges in the graph (solid black lines). A source node (blue) and a target node (red) are also included into the graph to include boundary conditions and flow direction.

between DFN and graph naturally assigns fracture-based properties, both geometric and hydrological, as node attributes. Edges are assigned unit weight to isolate topological attributes from other attributes that could be considered.

Source and target nodes are included into the graph to incorporate flow direction. Every fracture that intersects the inlet plane is connected to the source node and every fracture that intersects to the outlet plane is connected to the target node. The inclusion of flow direction is essential to identify possible transport locations, which depend upon the imposed pressure gradient [34]. An example of this mapping for a three-dimensional twelve fracture network is shown in figure 2. Each of the fractures (semi-transparent colored planes) are represented as nodes (black), intersections between fractures are represented by edges in the graph (solid black lines). The source node is colored blue and the target node is colored red.

Every subgraph has a unique pre-image in the fracture network that is a subnetwork of the full network because the mapping between the network and graph is bijective. Thus, flow and transport simulations can be performed on these subnetworks, and compared to results obtained on the full networks.

3.2 Node features

The centrality of a node in a graph describes how important it is to transport across the network. We consider four centrality measures as node features and predictors of flow. Three are global topological measures, quantifying how frequently paths through the graph include a given node. One is a local topological measure, measuring the number of immediate neighbors of a given

node. Graph properties are computed using the NETWORKX graph software package [15]. The topological features are supplemented with two physical (geometric) features; fracture volume projected along the main flow axis (from inlet plane to outlet plane) and fracture permeability. Figure 3 provides a visualization of a graph derived from the random DFN shown in Figure 1. Blue circles represent normalized feature values using these six different features, in panels a) through f). The yellow square and circle denote the source and target. Heavy lines represent particle backbone paths in the graphs.

3.2.1 Global topological features

- The *betweenness centrality* [5, 12] of a node (Figure 3a) reflects the extent to which that node can control communication on a network. Consider a geodesic path (path with fewest possible edges) connecting a node u and a node v on a graph. In general, there may be more than one such path: let σ_{uv} denote the number of them. Furthermore, let $\sigma_{uv}(i)$ denote the number of such paths that pass through node i . We then define, for node i ,

$$\text{Betweenness centrality} = \frac{1}{(n-1)(n-2)} \sum_{\substack{u,v=1 \\ u \neq i \neq v}}^n \frac{\sigma_{uv}(i)}{\sigma_{uv}}, \quad (1)$$

where the leading factor normalizes the quantity so that it can be compared across graphs of different sizes n . Figure 3a confirms that many backbone nodes do indeed have high betweenness values. At the same time, certain paths through the network that are not part of the backbone also show high values for this feature, reflecting that betweenness centrality considers *all* paths in the graphs, and not only those from source to target.

- *Source-to-target current flow* (Figure 3b) is a centrality measure based on an electrical current model [7], and assumes a given source and target. Imagine that one unit of current is injected into the network at the source, one unit is extracted at the target, and every edge has unit resistance. Then, the current flow centrality is equal to the current passing through a given node. This is given by Kirchhoff's laws, or alternatively in terms of the graph Laplacian matrix $\mathbf{L} = \mathbf{D} - \mathbf{A}$, where \mathbf{A} is the adjacency matrix for the graph and \mathbf{D} is a (diagonal) matrix specifying node degree: $D_{ii} = \sum_j A_{ij}$. Letting \mathbf{L}^+ denote the Moore-Penrose pseudoinverse of \mathbf{L} , s the source node, and t the target node, then for node i we define

$$\text{Current flow} = \sum_{j=1}^n A_{ij} |(L_{is}^+ - L_{js}^+) - (L_{it}^+ - L_{jt}^+)|. \quad (2)$$

Current-flow centrality is also known as random-walk centrality [35], since the same quantity measures how often a random walk from s to t passes through i . Unlike betweenness centrality, the current-flow centrality is zero on any branch of the graph outside of the central core. We therefore expect

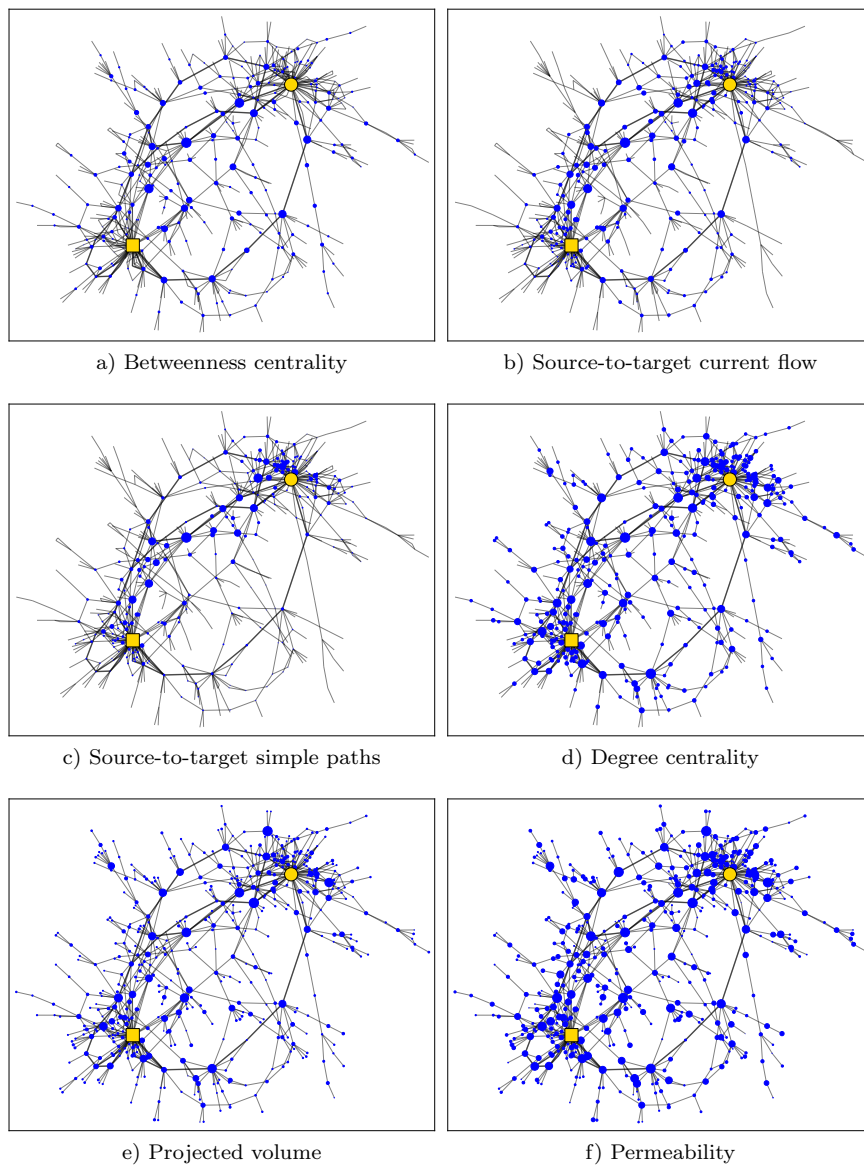


Fig. 3 Visualization of a graph derived from a random DFN as shown in Figure 1. Blue circles represent normalized feature values using six different features, in panels a) through f). Yellow square denotes source, yellow circle denotes target. Heavy lines represent particle backbone paths in the graphs. Note varying extent of correlation between particle backbone and associated feature strength.

high current flow values to correlate with nodes that have large influence on source-to-target transport.

- *Source-to-target simple paths* (Figure 3c) is a centrality measure that counts simple (non-backtracking) paths crossing the graph from source s to target t . Let π_{st} denote the number of such paths, and $\pi_{st}(i)$ denote the number of those passing through node i . We then define, for node i ,

$$\text{Simple paths} = \frac{\pi_{st}(i)}{\pi_{st}}, \quad (3)$$

where normalization by π_{st} allows comparing values of simple path centrality across different graphs. Due to the exponential proliferation of possible paths, we limit our search to paths with 15 nodes or less. Beyond 15, the effect on source-to-target simple path centrality is negligible. Figure 3c illustrates that nodes with high simple path centrality are more likely to lie on backbone paths than are nodes with high betweenness centrality in Figure 3a. However, simple path centrality also fails to identify one isolated backbone path that is disjoint from the others.

3.2.2 Local topological feature

- *Degree centrality* (Figure 3d) is a normalized measure of the number of edges touching a node. For node i ,

$$\text{Degree centrality} = \frac{1}{n-1} \sum_{j=1}^n A_{ij}. \quad (4)$$

Nodes with high degree centrality tend to be concentrated in the core of the network. Conversely, nodes with low degree centrality are often in the periphery or on branches that cannot possibly conduct significant flow. Physically, degree centrality of a fracture is the number of other fractures that intersect with it.

3.2.3 Physical features

We supplement the four topological features with two features describing physical properties of fractures.

- *Projected volume* (Figure 3e) measures the component of a fracture's volume oriented along the direction of flow from inlet to outlet plane. Let fracture i have volume V_i and orientation vector \mathbf{O}_i (unit vector normal to the fracture plane). Taking flow to be oriented along the x -axis, the projected volume is expressed by the projection of \mathbf{O}_i onto the yz -plane:

$$\text{Projected volume} = V_i \sqrt{(O_i)_y^2 + (O_i)_z^2}. \quad (5)$$

Figure 3e shows similarities between this feature and degree centrality, but also some fractures where one feature correlates more closely with the backbone than the other.

- *Permeability* (Figure 3f) measures how easily a porous medium allows flow. Given the aperture size b_i of fracture i , the permeability is expressed as

$$\text{Permeability} = \frac{b_i^2}{12} \quad (6)$$

The permeability of a fracture, which is nonlinearly related to its volume, is a measure of its transport capacity. As illustrated in Figure 3, it displays similarities to both degree centrality and projected volume, with backbone fractures almost systematically having high permeability values (but the converse holding less consistently).

3.3 Correlation of feature values

As is seen in Figure 3, the feature values vary widely from one node to another in ways that we aim to manipulate in order to predict backbone paths. Figure 4 shows correlation coefficients for pairs that include the particle backbone and the six features that we have chosen. That there are non-negligible correlations between the backbone and these features suggests that they are

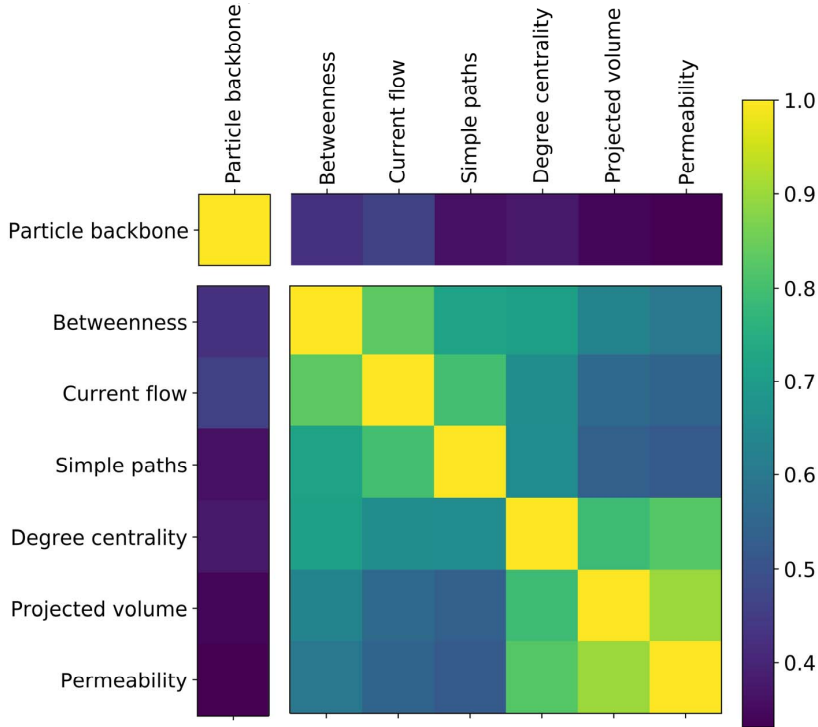


Fig. 4 Heat map displaying correlations among the particle backbone and the six features used.

relevant ones for classification, although clearly no single feature is sufficient in itself. The correlation coefficients indicate that features tend to cluster naturally into the three categories above. The first three features, which are the global topological ones (betweenness, current flow, and simple paths), have significant mutual correlations among them. The same is true for the physical features (projected volume and permeability), which also exhibit some clustering with the related local topological feature (degree centrality). The latter correlations are consistent with our feature definitions above.

4 Classification Methods

In this section, we explain how we evaluate classification performance, briefly describe our two machine learning algorithms (random forest and support vector machines), and our process for parameter selection. Both algorithms are general-purpose supervised learning methods suitable both for geometric and non-geometric features. Given a set of features and class assignment for some observations, supervised learning algorithms try to “learn” the underlying function that maps features to classes. Those observations are the training set. Once learned, the function can then be used to classify new observations. In our study, we use as observations the nodes (fractures) from 80 graphs as a training set. We then test the function using nodes from 20 graphs as a test set. Both algorithms are implemented using the *scikit-learn* machine learning package in python, with the functions *RandomForestClassifier* and *SVC*.

4.1 Performance measures

In our classification problem, there is a large class imbalance. Only about 7 percent of nodes in the training set are in the backbone. This presents a challenge in evaluating classification performance. A classifier could simply assign all nodes to the non-backbone class, and still achieve an overall accuracy of 93 percent. Careful attention to performance measures is therefore needed.

We define a *positive* classification of a node as being an assignment to the backbone class, and a *negative* classification as being an assignment to the non-backbone class. True positives (TP) and true negatives (TN) represent nodes whose backbone/non-backbone assignment matches that of the labeled training data. False positives (FP) and false negatives (FN) represent nodes whose backbone/non-backbone assignment is opposite that of the labeled training data. One straightforward measure of success is the TP rate. *Precision* and *recall* represent two kinds of TP rates:

$$\text{Precision} = \frac{TP}{TP + FP} \quad (7)$$

$$\text{Recall} = \frac{TP}{TP + FN} \quad (8)$$

Precision is the number of true positives over the total number that we classify as positive, whereas recall is the number of true positives over the total number of actual positives. These values give an understanding of how reliable (precision) and complete (recall) our results are.

There is generally a tradeoff between precision and recall. This can be seen in the behavior of one of the simplest possible forms of classification: thresholding according to a single feature. Consider a classifier that labels as backbone all fractures with nonzero current flow. The process would resemble the dead-end fracture chain removal method common in the hydrology literature, but more extreme in that it would eliminate all dead-end subnetworks. This gives perfect (100%) recall, since all fractures in the particle backbone necessarily have nonzero current flow, and 15% precision, as it reduces the network to about half of its original size. Now imagine increasing the threshold, so as to lower the number of positive assignments. This will reduce FP, thereby increasing the precision. However, it will also increase FN, reducing the recall. In this way, we can travel along a precision/recall curve, shown in Figure 5, that has perfect recall as one extreme and perfect precision as the other. If there existed a threshold value at which the classifier recovered the training data perfectly, the precision/recall curve would touch the upper-right corner of the figure: 100% precision and 100% recall. One typically wants classifiers that come as close to that ideal as possible.

Even though we train our classifier according to the particle backbone, however, our objective is not necessarily a perfect recovery of that structure. We aim to identify fractures that are a small subset of the full network, but nevertheless conduct significant flow and provide good agreement with the full network's breakthrough curve, describing the distribution of times for particles

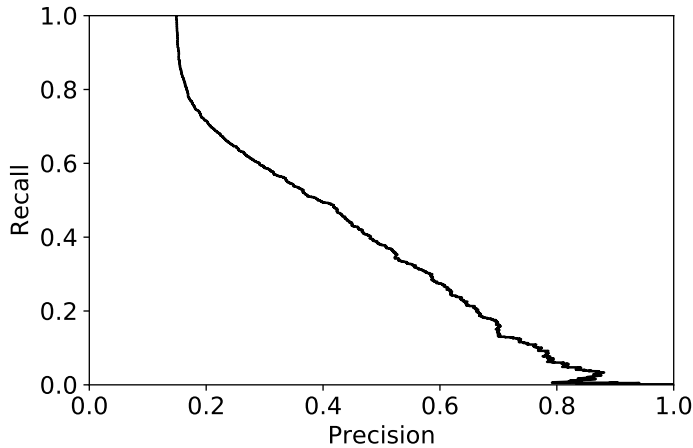


Fig. 5 Precision/recall curve for current-flow thresholding as a classifier. As threshold value increase, classifier moves from perfect recall to perfect precision. Classifiers with precision/recall curves touching upper-right corner have strongest performance.

to pass through the network. Many, but not all, of the fractures in the particle backbone are essential for this purpose. Thus, high recall is needed, though not necessarily perfect recall. Precision is less essential: false positives will increase the size of our remaining network, but even low precision could allow for a significant reduction in number of fractures.

4.2 Random forest

A random forest [16,17] is constructed by sampling the training set with replacement, so that some data points may be sampled multiple times and others not at all. Those data points that are sampled are used to generate a large collection of decision trees, each of which outputs a classification based on feature values. Those data points that are not sampled are run through the decisions trees. A test data point is then classified by having each tree “vote” on its class. This leads not only to a predicted classification, but also to a measure of certainty (the fraction of trees that voted for it) as well as to an estimate of the importance of each feature for the class assignment [8]. That final estimate is particularly useful when the features consist of quantities that measure different aspects of node centrality.

In order to identify the parameters of random forest that affect our results most significantly, we use a grid search cross-validation method, implemented with the *GridSearchCV* function in *scikit-learn*. This method optimizes a classifier by exhaustive search within a given range of parameter values, recursively building and testing models. Given the class imbalance in our problem, we set the parameter ranges to aim for high recall. We find the greatest sensitivity to a parameter that sets the minimal number of samples in a leaf node, to limit how much a decision tree branches. Adjusting that number can prevent overfitting, which in the context of unbalanced classes could cause practically none of the feature space to be assigned to the minority class.

4.3 Support vector machines

Support vector machines (SVM) separate high-dimensional data points into two classes by finding an appropriate hyperplane. Based on the generalized portrait algorithm [46] and subsequent developments in statistical learning theory [45], the current version of SVM [9] uses kernel methods [6] to generalize linear classifiers to nonlinear ones. These enable SVM to perform well when certain feature variables are highly correlated or even unimportant to the class assignment [25], and help prevent overfitting. We therefore enlarge our feature space for SVM by ranking the values of each feature within a given graph, and use the six ranked features along with the six raw features.

As with random forest, we use grid search cross-validation to identify and optimize crucial parameters in SVM. We find the most important of these to be the penalty parameter C . When C is low, SVM is tolerant to misclassification

among the training data. Because of our class imbalance, we assign different penalty values for each class, so that the classifier more strictly bounds the (minority) backbone nodes than the (majority) non-backbone nodes. In this way, we can simultaneously prevent overfitting the majority class and “over-looking” points in the minority class. By adjusting the balance of penalty values, we control how likely the classifier is to assign a node to the backbone.

5 Results

We used a collection of 100 graphs. 80 were chosen as training data, and 20 were chosen as test data. We illustrate certain results, including breakthrough curves, on the DFN shown in Figure 1. Other results are based on the entire test set, which consists of a total of 9238 fractures, 651 of which (7.0%) are in the particle backbone and 8587 of which (93%) are not. The total computation time to train both RF and SVM was on the order of a minute, negligible compared to the time to extract the particle backbone needed for training. Once trained, the classifier ran on each test graph in seconds.

5.1 Classifiers

We implemented random forest using the *RandomForestClassifier* function in *scikit-learn*, on the six features described in Section 3.2. Parameters were set to default values, except as follows: 250 trees were used ($n_estimators=250$), the number of features to consider for the best split was given by the binary logarithm of the number of trees ($max_features=log2$), and information gain was used to measure the quality of a split ($criterion='entropy'$). To compensate for class imbalance, we also used voting weights inversely proportional to class frequency ($class_weight='balanced_subsample'$). Table 1 gives the results from the classifiers generated with four different values of minimal number of training samples in a leaf node ($min_samples_leaf$). Since the full particle backbone accounts for only 7% of the fractures in the test set, we see that even classifiers with relatively low precision can reduce the network significantly.

Random forest also provides a quantitative estimate of the relative importance of each of the six features described in Section 3.2, based on how often a tree votes for it. Using the RF(30) model on our 80 training graphs, we find

Classifier	Precision	Recall	Fractures remaining
RF(1400)	18%	90%	36%
RF(30)	26%	75%	21%
RF(15)	30%	65%	15%
RF(1)	58%	20%	2.5%

Table 1 Random forest classifiers labeled by the $min_samples_leaf$ parameter value, controlling how much a decision tree can branch. Percentages for precision, recall, and fractures remaining in network are calculated over all 20 graphs in the test set.

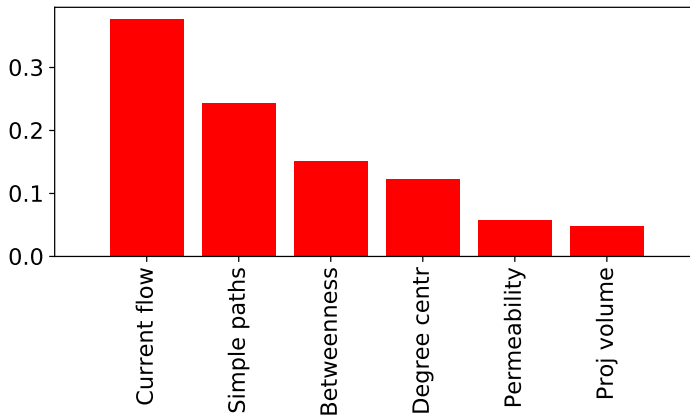


Fig. 6 Relative importances of features based on training data for random forest.

the feature importances shown in Figure 6. The source-to-target current flow, source-to-target simple paths, and betweenness centralities are the most important features, followed by node degree, and followed finally by permeability and projected volume. Thus, as with the feature correlations shown in Figure 4, the feature importances cluster into three natural groups. Global topological features have the greatest importance, local topological features have significant but lower importance, and physical features play only a small role in classification. In contrast with SVM, the performance of random forest does not benefit from using additional features such as ranked values. The inherent bootstrapping of random forest enables strong classification performance even with a relatively limited number of features.

We implemented SVM using the *SVC* function in *scikit-learn*, on twelve features made up of the six raw features described in Section 3.2 as well as their ranked counterparts. We chose a penalty of $C = 0.01$, weighted by additional coefficients (*class_weight*) for each class that we adjusted in order to vary precision and recall. This resulted in a pair of C values for the backbone and non-backbone classes. Table 2 gives the results from the classifiers generated with four different pairs of penalty values. All other parameters were set to their default values, which include a radial kernel (closed decision boundary).

Classifier	Precision	Recall	Fractures remaining
SVM(0.90,0.054)	17%	96%	39%
SVM(0.90,0.063)	19%	90%	34%
SVM(0.70,0.070)	23%	78%	24%
SVM(0.70,0.190)	44%	46%	7.3%

Table 2 SVM classifiers labeled by the misclassification penalty for the backbone class and the non-backbone class. The parameter for a class is equal to C multiplied by its class weight. Percentages for precision, recall, and fractures remaining in network are calculated over all 20 graphs in the test set.

5.2 Validation

In order to evaluate the quality of our classification results, we illustrate two cases on the DFN from Figure 1. In Figure 7 (a), we visualize the result of our classifier with the highest recall and lowest precision, SVM(0.90,0.054). Here, most of the nodes in the particle backbone are classified as positive.

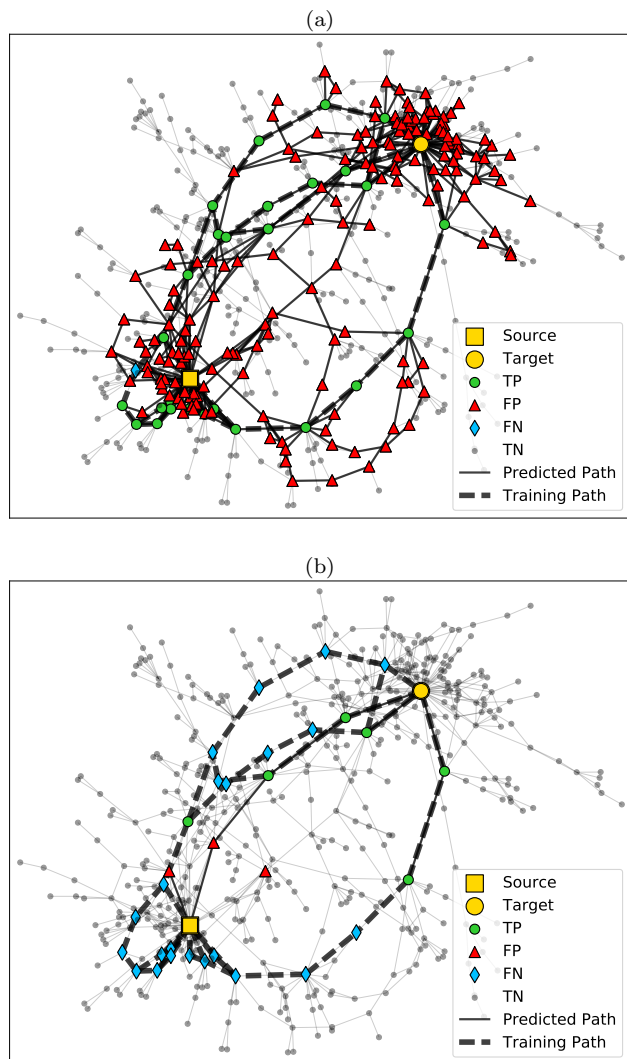


Fig. 7 Extreme cases of classification results: (a) SVM(0.90,0.054) with high recall and low precision (40% of network remaining), showing many false positives (FP) and relatively few false negatives (FN), and (b) RF(1) with low recall and high precision (2% of network remaining), showing many false negatives (FN) and relatively few false positives (FP). Solid lines show predicted paths from source to target. Dashed lines show particle backbones.

The few false negatives (FN) are near the source, and are primarily fractures intersecting the source plane where high particle concentrations accumulate. False positives (FP) are far more prevalent, forming many connected source-to-target paths that are not in the particle backbone. In spite of these, the reduced network identified by the classifier contains only 40% of the original fractures.

In Figure 7 (b), we visualize the result of our classifier with the highest precision and lowest recall, RF(1). We see almost no false positives (FP), but most of the nodes in the particle backbone are missed. While the false negatives (FN) near the source are not necessarily of great concern, as these simply represent the inlet plane, it is notable that only one connected path exists between source and target. On some other networks in the test set, the classifier does not even generate a connected source-to-target path at all. The drastic reduction of network size, to 2% of the original fractures, results in too much loss of physical relevance.

It is instructive to consider the full range of precision and recall values for the classifiers above, as we did for the simple current-flow thresholding method in Section 4. Given a trained classifier, one can modify it to give more or fewer positive assignments, effectively changing the percentage of votes needed for a positive classification (in the case of RF) or shifting the decision boundary (in the case of SVM). Note that this is not the same as generating different classifiers from the training data, as in Tables 1 and 2. Figure 8 shows precision/recall curves generated in this way for the two classifiers used in Figure 7, along with the current-flow curve as a baseline comparison. Marker values represent the precision/recall values seen in Tables 1 and 2 for the unmodified classifiers. It appears at first that current-flow thresholding has the strongest performance below about 60% recall. However, as with RF(1)

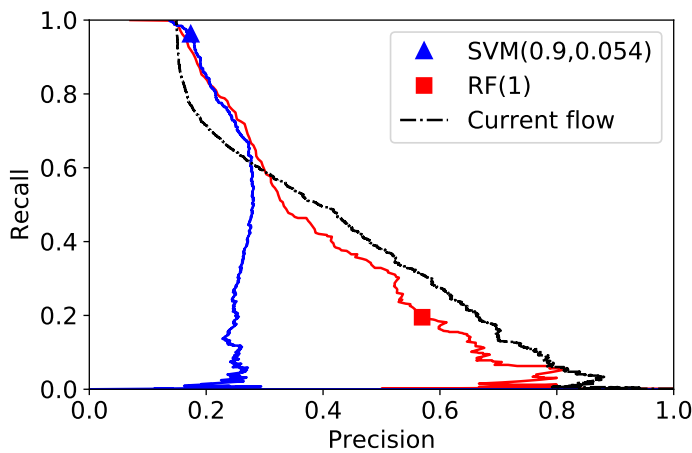


Fig. 8 Precision/recall obtainable with one SVM and one RF classifier, along with current-flow thresholding for comparison. Markers indicate performance of unmodified classifier.

above, it can give nonphysical results: in fact, for all but the highest recall values (current-flow thresholds near 0), it generates a disconnected backbone.

Moreover, our ultimate objective is not reconstructing training data, but rather reducing the network size while maintaining crucial flow properties. These properties are measured by the breakthrough curve (BTC), which gives the distribution of simulated particles passing through the network from source plane to target plane in a given interval of time. This is a common quantify of interest in subsurface systems, where one needs to predict the travel time distribution through the fracture network in order to evaluate the performance of systems such as hydraulic fracturing, nuclear waste disposal or gas migration from a nuclear test. We would like the BTC for our reduced networks to match that of the full network in a number of respects, notably the shape of the cumulative distribution function and the fraction of particles that reach the target plane after a given time. While the particle backbone is important for identifying where mass transports through the network, it is only one of many valid network reductions from the perspective of characterizing flow.

Figure 9 shows the BTC on this network for a representative sample of four of our classifiers. As a comparison, we also show the BTC for thresholding on nonzero current flow, as well as for the full network and for the particle backbone. While current flow thresholding gives a very close match, it only reduces

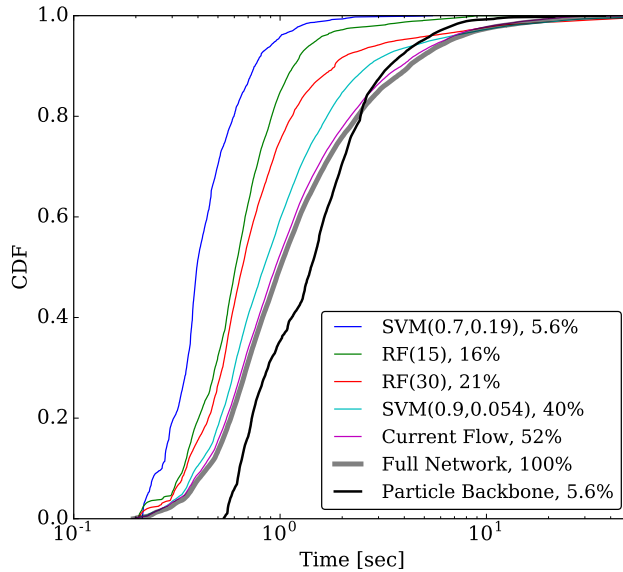


Fig. 9 Predictions for the DFN from Figure 1, visualized as BTC (cumulative distribution function) produced by DFNWORKS. Representative results from four models are given, together with current-flow thresholding, full network and particle backbone. Legend shows model parameters and size of reduced network.

the network to 52% of its original size. SVM(0.9,0.054) and RF(30) reduce the network to 40% and 21%, while still providing acceptable matches. The median breakthrough time for RF(30) deviates from that of the full network by approximately the same amount as the particle backbone, though in the opposite direction: it underestimates rather than overestimates the breakthrough time.

Finally, in order to quantify the tradeoff between BTC agreement and network reduction, we calculate the Kolmogorov-Smirnov (KS) statistic, giving a measure of “distance” between two probability distributions. The KS statistic is independent of binning, and most sensitive to discrepancies close to the medians of the distributions, making it particularly suitable for comparing BTCs. The results are summarized in Table 3. They confirm that the classifier with highest recall, SVM(0.90,0.054), which reduces the network to 40% of its original size, has a BTC close to that of the full network (KS statistic 0.10).

Classifier	Fractures remaining	KS
Current flow	52%	0.03
SVM(0.90,0.054)	40%	0.10
RF(1400)	38%	0.12
SVM(0.90,0.063)	35%	0.12
SVM(0.70,0.070)	22%	0.25
RF(30)	21%	0.26
RF(15)	16%	0.35
SVM(0.70,0.190)	5.6%	0.59
RF(1)	2.0%	0.68

Table 3 Results of applying current-flow thresholding, four RF and four SVM models to the DFN from Figure 1. Fractures remaining in network are those identified as backbone by classifier. Values differ slightly from results over entire test set, due to graph-to-graph fluctuations. KS statistic represents distance between breakthrough curve on reduced network and on full network.

6 Discussion and Conclusions

We have presented a novel approach to finding a backbone subnetwork that does not require resolving flow in the network, and that takes minimal computational time. The method involves representing a DFN as a graph whose nodes represent fractures, and applying machine learning techniques to rapidly predict which nodes are part of the backbone. We used two supervised learning techniques: random forest and support vector machines. Once these algorithms have been trained on flow data from particle simulations, they successfully reduce new DFNs to subnetworks that preserve crucial flow properties. Our algorithms use topological features associated with nodes on the graph, as well as a small number of physical features describing a fracture’s properties. We consider each node as a point in the multi-dimensional feature space, and classify it according to whether or not it belongs to the backbone.

By varying the parameters of our classifiers, we are able to obtain a wide range of precision and recall values. These yield backbones whose sizes range from 40% down to 2% of the original network. For reductions as small as 21% of the original size, the resulting breakthrough curve (BTC) displays good agreement with that of the original network. We therefore obtain subnetworks that are significantly smaller than the full network, useful for flow simulations, and generated in seconds. By comparison, the computation time needed to extract the particle backbone is on the order of hours.

In addition to the classification results, the random forest method gives a set of relative importances for the features used. These importances are determined by permuting the values of a given feature and observing the effect this has on classification performance. We have found that features based on global topological properties of the underlying graph were significantly more important than those based on geometry or physical properties of the fractures. This reinforces previous observations that network connectivity is more fundamental to determining flow than are geometric or hydraulic properties [20]. Quantitatively, the most important of our global topological features is source-to-target current flow, which measures how much of a unit of current injected at the source (representing the inlet plane of the DFN) passes through a given node of the graph.

Indeed, classifying fractures only based on whether they conduct nonzero current flow yields in itself a reasonable graph reduction of around 50%, with a BTC that very closely matches the original network. However, this does not generalize to a method allowing arbitrary graph reduction: raising the current-flow threshold above zero reduces the number of fractures, but results in networks that are disconnected and therefore nonphysical. By contrast, when we use the full set of classification features, we consistently realize a connected backbone for all but the lowest recall values. It is somewhat remarkable that this occurs in spite of our classifiers never explicitly making use of source-to-target paths in the graph.

Finally, some evidence suggests that if one could in fact generate backbone paths rather than backbone nodes, results would improve further. We are currently exploring a classification method that initially labels fractures at the inlet and outlet planes, and then successively attempts to propagate fractures labeled as backbone through the network, thereby forming source-to-target paths. The objective of this method is to generate subnetworks that are far closer to the particle backbone itself. Thus, the training data would be used not merely to guide the classifier toward useful network reductions, but rather in the more conventional machine learning setting of providing ground truth to be reproduced. Preliminary tests suggest that such a method may considerably boost precision and recall simultaneously, generating subnetworks whose BTC closely matches the full network but whose size is not much larger than the particle backbone.

7 Acknowledgments

This work was supported by the Computational Science Research Center at San Diego State University, the National Science Foundation Graduate Research Fellowship Program under Grant No. 1321850, and the U.S. Department of Energy at Los Alamos National Laboratory under Contract No. DE-AC52-06NA25396 through the Laboratory Directed Research and Development program. JDH thanks the LANL LDRD Director's Postdoctoral Fellowship Grant # 20150763PRD4 for partial support. JDH, HSV, and GS thank LANL LDRD-DR Grant #20170103DR for support.

References

1. Abelin, H., Birgersson, L., Moreno, L., Widén, H., Ågren, T., Neretnieks, I.: A large-scale flow and tracer experiment in granite: 2. results and interpretation. *Water Resour. Res.* **27**(12), 3119–3135 (1991)
2. Abelin, H., Neretnieks, I., Tunbrant, S., Moreno, L.: Final report of the migration in a single fracture: experimental results and evaluation. *Nat. Genossenschaft fd Lagerung Radioaktiver Abfälle* (1985)
3. Aldrich, G., Hyman, J., Karra, S., Gable, C., Makedonska, N., Viswanathan, H., Woodring, J., Hamann, B.: Analysis and visualization of discrete fracture networks using a flow topology graph. *IEEE T. Vis. Comput. Gr.* (2016)
4. Andresen, C.A., Hansen, A., Le Goc, R., Davy, P., Hope, S.M.: Topology of fracture networks. *Frontiers in Physics* **1**(August), 1–5 (2013). DOI 10.3389/fphy.2013.00007. URL <http://www.frontiersin.org/Journal/10.3389/fphy.2013.00007/full>
5. Anthonisse, J.: The rush in a directed graph. *Stichting Mathematisch Centrum. Mathematische Besliskunde (BN 9/71)*, 1–10 (1971). URL <http://www.narcis.nl/publication/RecordID/oai%7B%3Acwi.nl%7D%3A9791>
6. Boser, B.E., Guyon, I.M., Vapnik, V.N.: A training algorithm for optimal margin classifiers. *Proceedings of the fifth annual workshop on Computational learning theory COLT'92* p. 144 (1992). DOI 10.1145/130385.130401
7. Brandes, U., Fleischer, D.: Centrality measures based on current flow. *Proc. 22nd Symp. Theoretical Aspects of Computer Science* **3404**, 533–544 (2005)
8. Breiman, L.: Random forests. *Machine Learning* **45**(1), 5–32 (2001). DOI 10.1023/A:1010933404324
9. Cortes, C., Vapnik, V.: Support-vector networks. *Machine Learning* **20**(3), 273–297 (1995). DOI 10.1007/BF00994018
10. de Dreuzy, J.R., Méheust, Y., Pichot, G.: Influence of fracture scale heterogeneity on the flow properties of three-dimensional discrete fracture networks. *J. Geophys. Res.-Sol. Ea.* **117**(B11) (2012)
11. Frampton, A., Cvetkovic, V.: Numerical and analytical modeling of advective travel times in realistic three-dimensional fracture networks. *Water Resour. Res.* **47**(2) (2011)
12. Freeman, L.C.: A set of measures of centrality based on betweenness. *Sociometry* **40**(1), 35–41 (1977)
13. Ghaffari, H.O., Nasser, M.H.B., Young, R.P.: Fluid flow complexity in fracture networks: Analysis with graph theory and LBM. *ArXiv e-prints* p. 1107.4918 (2011)
14. Goetz, J.N., Brenning, A., Petschko, H., Leopold, P.: Evaluating machine learning and statistical prediction techniques for landslide susceptibility modeling. *Computers and Geosciences* **81**, 1–11 (2015)
15. Hagberg, A.A., Schult, D.A., Swart, P.: Exploring network structure, dynamics, and function using networkx. In: *Proceedings of the 7th Python in Science Conferences (SciPy 2008)*, vol. 2008, pp. 11–16 (2008)
16. Ho, T.K.: Random decision forests. *Proceedings of the 3rd International Conference on Document Analysis and Recognition* **14-16**, 278–282 (1995)

17. Ho, T.K.: The random subspace method for constructing decision forests. *IEEE Transactions on Pattern Analysis and Machine Intelligence* **20**(8), 832–844 (1998). DOI 10.1109/34.709601
18. Hope, S.M., Davy, P., Maillot, J., Le Goc, R., Hansen, A.: Topological impact of constrained fracture growth. *Frontiers in Physics* **3**(September), 1–10 (2015). DOI 10.3389/fphy.2015.00075. URL <http://journal.frontiersin.org/article/10.3389/fphy.2015.00075>
19. Hyman, J., Jiménez-Martínez, J., Viswanathan, H., Carey, J., Porter, M., Rougier, E., Karra, S., Kang, Q., Frash, L., Chen, L., et al.: Understanding hydraulic fracturing: a multi-scale problem. *Phil. Trans. R. Soc. A* **374**(2078), 20150426 (2016)
20. Hyman, J.D., Aldrich, G., Viswanathan, H., Makedonska, N., Karra, S.: Fracture size and transmissivity correlations: Implications for transport simulations in sparse three-dimensional discrete fracture networks following a truncated power law distribution of fracture size. *Water Resources Research* **52**(8), 6472–6489 (2016). DOI 10.1002/2016WR018806. URL <http://dx.doi.org/10.1002/2016WR018806>
21. Hyman, J.D., Gable, C.W., Painter, S.L., Makedonska, N.: Conforming Delaunay triangulation of stochastically generated three dimensional discrete fracture networks: A feature rejection algorithm for meshing strategy. *SIAM J. Sci. Comput.* **36**(4), A1871–A1894 (2014)
22. Hyman, J.D., Hagberg, A., Srinivasan, G., Mohd-Yusof, J., Viswanathan, H.S.: Accurate and efficient predictions of first passage times in sparse discrete fracture networks using graph-based reductions. *Phys. Rev. E (Under Review)* (2017)
23. Hyman, J.D., Karra, S., Makedonska, N., Gable, C.W., Painter, S.L., Viswanathan, H.S.: dfnWorks: A discrete fracture network framework for modeling subsurface flow and transport. *Computers and Geosciences* **84**, 10–19 (2015). DOI 10.1016/j.cageo.2015.08.001. URL <http://dx.doi.org/10.1016/j.cageo.2015.08.001>
24. Hyman, J.D., Painter, S.L., Viswanathan, H., Makedonska, N., Karra, S.: Influence of injection mode on transport properties in kilometer-scale three-dimensional discrete fracture networks. *Water Resour. Res.* **51**(9), 7289–7308 (2015)
25. James, G., Witten, D., Hastie, T., Tibshirani, R.: *An Introduction to Statistical Learning*. Springer (2013)
26. Jenkins, C., Chadwick, A., Hovorka, S.D.: The state of the art in monitoring and verification—ten years on. *Int. J. Greenh. Gas. Con.* **40**, 312–349 (2015)
27. Karra, S., Makedonska, N., Viswanathan, H., Painter, S., Hyman, J.: Effect of advective flow in fractures and matrix diffusion on natural gas production. *Water Resources Research* **51**, 1–12 (2014)
28. LaGriT: Los Alamos Grid Toolbox, (LaGriT) Los Alamos National Laboratory. <http://lagrit.lanl.gov> (2013)
29. Lichtner, P., Hammond, G., Lu, C., Karra, S., Bisht, G., Andre, B., Mills, R., Kumar, J.: PFLOTRAN user manual: A massively parallel reactive flow and transport model for describing surface and subsurface processes. Tech. rep., (Report No.: LA-UR-15-20403) Los Alamos National Laboratory (2015)
30. Maillot, J., Davy, P., Le Goc, R., Darcel, C., De Dreuzy, J.R.: Connectivity, permeability, and channeling in randomly distributed and kinematically defined discrete fracture network models. *Water Resources Research* **52**(11), 8526–8545 (2016)
31. Makedonska, N., Painter, S.L., Bui, Q.M., Gable, C.W., Karra, S.: Particle tracking approach for transport in three-dimensional discrete fracture networks. *Computat. Geosci.* pp. 1–15 (2015)
32. Mudunuru, M.K., Karra, S., Makedonska, N., Chen, T.: Joint geophysical and flow inversion to characterize fracture networks in subsurface systems. *ArXiv e-prints* p. 1606.04464 (2016)
33. National Research Council: *Rock fractures and fluid flow: contemporary understanding and applications*. National Academy Press (1996)
34. Neuman, S.: Trends, prospects and challenges in quantifying flow and transport through fractured rocks. *Hydrogeol. J.* **13**(1), 124–147 (2005)
35. Newman, M.: A measure of betweenness centrality based on random walks. *Social Networks* pp. 39–54 (2005)
36. Painter, S., Cvetkovic, V.: Upscaling discrete fracture network simulations: An alternative to continuum transport models. *Water Resour. Res.* **41**, W02,002 (2005)

37. Painter, S., Cvetkovic, V., Selroos, J.O.: Power-law velocity distributions in fracture networks: Numerical evidence and implications for tracer transport. *Geophys. Res. Lett.* **29**(14) (2002)
38. Painter, S.L., Gable, C.W., Kelkar, S.: Pathline tracing on fully unstructured control-volume grids. *Computat. Geosci.* **16**(4), 1125–1134 (2012)
39. Rasmuson, A., Neretnieks, I.: Radionuclide transport in fast channels in crystalline rock. *Water Resour. Res.* **22**(8), 1247–1256 (1986)
40. Robinson, B.A., Dash, Z.V., Srinivasan, G.: A particle tracking transport method for the simulation of resident and flux-averaged concentration of solute plumes in groundwater models. *Computational Geosciences* **14**(4), 779–792 (2010)
41. Santiago, E., Romero-Salcedo, M., Velasco-Hernández, J.X., Velasquillo, L.G., Hernández, J.A.: An integrated strategy for analyzing flow conductivity of fractures in a naturally fractured reservoir using a complex network metric. In: I. Batyrshin, M.G. Mendoza (eds.) *Advances in Computational Intelligence: 11th Mexican International Conference on Artificial Intelligence, MICAI 2012, San Luis Potosí, Mexico, October 27 – November 4, 2012. Revised Selected Papers, Part II*, pp. 350–361. Springer, Berlin, Heidelberg (2013)
42. Santiago, E., Velasco-Hernández, J.X., Romero-Salcedo, M.: A methodology for the characterization of flow conductivity through the identification of communities in samples of fractured rocks. *Expert Systems With Applications* **41**(3), 811–820 (2014). DOI 10.1016/j.eswa.2013.08.011. URL <http://dx.doi.org/10.1016/j.eswa.2013.08.011>
43. Santiago, E., Velasco-Hernandez, J.X., Romero-Salcedo, M.: A descriptive study of fracture networks in rocks using complex network metrics. *Computers and Geosciences* **88**, 97–114 (2016). DOI 10.1016/j.cageo.2015.12.021
44. Srinivasan, G., Tartakovsky, D.M., Dentz, M., Viswanathan, H., Berkowitz, B., Robinson, B.: Random walk particle tracking simulations of non-fickian transport in heterogeneous media. *J. Comput. Phys.* **229**(11), 4304–4314 (2010)
45. Vapnik, V., Chervonenkis, A.Y.: *Theory of pattern recognition: Statistical problems of learning [in russian]* (1974)
46. Vapnik, V., Lerner, A.: Pattern recognition using generalized portrait method. *Automation and Remote Control* **24**, 774–780 (1963)
47. Veatne, J.N., Rimstad, E., Hope, S.M., Korsnes, R., Hansen, A.: Fracture networks in sea ice. *Frontiers in Physics* **2**, 1–8 (2014). DOI 10.3389/fphy.2014.00021
48. Witherspoon, P.A., Wang, J., Iwai, K., Gale, J.: Validity of cubic law for fluid flow in a deformable rock fracture. *Water Resour. Res.* **16**(6), 1016–1024 (1980)

Flow Equations and transport simulations

We assume that the matrix surrounding the fractures is impermeable and there is no interaction between flow within the fractures and the solid matrix. Within each fracture, flow is modeled using the Darcy equation

$$\mathbf{q} = -\frac{k}{\mu} \nabla P \quad (9)$$

where \mathbf{q} is the Darcy flux, k is the fracture permeability, μ is the fluid viscosity, and ∇P it the pressure gradient. The aperture within each fracture is uniform and isotropic, but they do vary between fractures and are positively correlated to the fracture size [20]. Locally, we adopt the cubic law [48] to relate the permeability of each fracture to its aperture. We drive flow through the domain by applying a pressure difference of 1MPa across the domain aligned with the x-axis. No flow boundary conditions are applied along lateral boundaries and gravity is not included in these simulations. These boundary conditions

along with mass conservation and equation (9) are used to form an elliptic partial differential equation for steady-state distribution of pressure within each network

$$\nabla \cdot (k \nabla P) = 0 . \quad (10)$$

Once the distribution of pressure and volumetric flow rates are determined by numerically integrating (10) the methodology of Makedonska et al. [31] and Painter et al. [38] and are used to determine the Eulerian velocity field $\mathbf{u}(\mathbf{x})$ at every node in the conforming Delaunay triangulation throughout each network.

The spreading of a nonreactive conservative solute transported is represented by a cloud of passive tracer particles, i.e., using a Lagrangian approach. The imposed pressure gradient is aligned with the x -axis and thus the primary direction of flow is in the x direction. Particles are released from locations in the inlet plane \mathbf{x}_0 at time $t = 0$ and are followed until the exit the domain at the outlet plane \mathbf{x}_L . The trajectory $\mathbf{x}(t; \mathbf{a})$ of a particle starting at \mathbf{a} on \mathbf{x}_0 is given by the advection equation, $\mathbf{x}(t; \mathbf{a}) = \mathbf{v}(t; \mathbf{a})$ with $\mathbf{x}(0; \mathbf{a}) = \mathbf{a}$ where the Lagrangian velocity $\mathbf{v}(t; \mathbf{a})$ is given in terms of the Eulerian velocity $\mathbf{u}(\mathbf{a})$ as $\mathbf{v}(t; \mathbf{a}) = \mathbf{u}[\mathbf{x}(t; \mathbf{a})]$. The mass represented by each particle $m(\mathbf{a})$ and the breakthrough time at the outlet plane, $\tau(\mathbf{x}_L; \mathbf{a})$ of a particle that has crossed the outlet plane, $\mathbf{x}_L = (L, y, z)$ is can be combined to compute the total solute mass flux $\psi(t)$ that has broken through at a time t ,

$$\Psi(t, \mathbf{x}_L) = \frac{1}{M} \int_{\Omega_a} dm(\mathbf{a}) \delta[t - \tau(\mathbf{x}_L, \mathbf{a})] , \quad (11)$$

where Ω_a is the set of all particles. Here mass is distributed uniformly amongst particles, i.e., resident injection is adopted. For more details about the injection mode see Hyman et al., [24].